



Degradation of the 2014–2015 Holuhraun vent-proximal edifice in Iceland

S. S. Sutton¹ · J. A. Richardson² · P. L. Whelley^{2,3} · S. P. Scheidt^{2,3} · C. W. Hamilton¹

Received: 8 September 2023 / Accepted: 11 January 2024 / Published online: 16 March 2024

This is a U.S. Government work and not under copyright protection in the US; foreign copyright protection may apply 2024

Abstract

The earliest stages of volcanic vent degradation are rarely measured, leaving a gap in the knowledge that informs landform degradation models of cinder cones and other monogenetic vent structures. We documented the initial degradation of a 500-m-long spatter rampart at the primary vent of the 2014–2015 Holuhraun eruption in northern Iceland with high-resolution topographic change maps derived from terrestrial laser scanning (TLS) and photogrammetric surveys using an unoccupied aircraft system (UAS). Topographic differencing shows a total negative volume change of 42,637 m³, and a total positive volume change (basal deposition) of 10,304 m³ (primarily as deposition at the base of steeply sloping surfaces). Two distinct styles of volume changes were observed on the interior and exterior of the spatter rampart. Material on the interior of the vent was removed from oversteepened slopes by discrete rockfalls, while diffusive processes were qualitatively evident on the exterior slopes. We propose a novel conceptual landform evolution model for spatter ramparts that combines rockfall processes on the interior walls, diffusive gravitational sliding on the exterior slopes, and incorporates cooling contraction and compaction over the entire edifice to describe the observed modes of topographic change during the onset of degradation. Potential hazards at fresh spatter ramparts are rockfalls at high slope areas of the vent interior walls where contacts between spatter clasts are prone to weakening by fumarolic activity, weathering, and settling. To capture such hazards, our data suggest a cadence for monitoring changes yearly for the first few years post-eruption, and at longer intervals thereafter.

Keywords Spatter rampart · Fissure vent · Topographic differencing · landform modeling · rockfalls

Introduction

Vent-proximal edifices, such as cinder and spatter cones, are characteristic products of monogenetic fissure eruptions. Models of cinder and spatter cone erosion have been used to estimate the ages of volcanic edifices and recurrence intervals (Wood 1980a, 1980b). However, these estimates rely on assumptions about the initial morphology of the edifice and

its degradation rate (Dohrenwend et al. 1986; Pelletier and Cline 2007; Keresztsuri et al. 2012; de Vitturi and Arrowsmith 2013), which can be problematic because direct measurements of the earliest stages of volcanic vent degradation are rarely measured (Bemis and Ferencz 2017). Moreover, the effects of spatter are not accounted for in the most widely used morphometric models, which assume that the structure is primarily composed of unconsolidated scoria (e.g. Porter 1972; Wood 1980a; Hooper and Sheridan 1998; Pelletier and Cline 2007). This paper addresses a gap in the knowledge of how spatter cones and spatter ramparts degrade within the first few years of their history.

To quantify the rates of vent-proximal edifice degradation, and constrain their causes, we documented time-series topographic changes spanning a 5-year period starting 6 months after the initial emplacement of the main spatter rampart at the source of the 2014–2015 Holuhraun eruption in central Iceland. We correlate the spatial distribution, types, and rates of topographic change with lithologic facies to explore how vent edifice construction influences

Editorial responsibility: A. Tibaldi

S. S. Sutton
ssutton@lpl.arizona.edu

¹ Lunar and Planetary Laboratory, University of Arizona,
1629 E. University Blvd., Tucson, AZ 85721, USA

² Planetary Geology, Geophysics and Geochemistry
Laboratory, NASA Goddard Space Flight Center, Greenbelt,
MD, USA

³ Department of Astronomy, University of Maryland College
Park, College Park, MD, USA

post-eruption degradation. We investigate factors intrinsic to volcanic processes—including agglutination, slope stability, subsidence, edifice cooling, and compaction. These observations inform a conceptual landform evolution model for the initial stages of the degradation of spatter ramparts that incorporates discrete rockfall events and slope diffusion with implications for improving existing models of cinder cone evolution (Keresztsuri et al. 2012; Fodor and Németh 2015) and age estimation (cf. Wood 1980b). Our results also have implications for interpreting the morphologies of fissure vent edifices on other planetary bodies (Hauber et al. 2009; Richardson et al. 2021). Additionally, the ability to relate the initial modes and rates of spatter cone or rampart degradation to emplacement processes and lava facies is relevant to hazard assessment by highlighting conditions associated with slope failure (González de Vallejo et al. 2020).

Spatter rampart construction

Spatter is a pyroclastic material produced during lava fountaining. Spatter deposits form when clots of erupted magma are hot enough to be deformable upon impact (Head and Wilson 1989; Sumner et al. 2005; Parfitt and Wilson 2009). Spatter clasts can stick to each other upon contact, becoming welded to different degrees, in a process called agglutination. If spatter accumulation rates are rapid enough, hot material will undergo compaction, thereby becoming strongly welded as boundaries between individual clasts to merge and become indistinguishable (Sumner et al. 2005). Spatter cones, as the name suggests, typically exhibit radial symmetry about a vent, whereas more elongated edifices are generally referred to as spatter ramparts (Bemis and Ferencz 2017). Low spatter ramparts may only be a few meters high and can form as semi-continuous units parallel to a fissure vent (Moore et al. 1980; Parcheta et al. 2012; Valentine et al. 2017), whereas larger spatter ramparts typically result from the coalescence of closely spaced cones that are centered along more productive segments of the source fissure (Witt et al. 2018).

Eruption characteristics such as lava discharge rate, magma gas content, existing topography, and wind speed and direction influence the edifice geometry and the strength of pyroclastic ramparts (Cas and Wright 2012; Keresztsuri et al. 2012). While there have been many studies that deal with the morphometry of cinder cones (e.g. Segerstrom 1956; Settle 1979; Wood 1980a, 1980b; Dohrenwend et al. 1986; Pelletier and Cline 2007; Fornaciai et al. 2010; Bemis et al. 2011; Keresztsuri et al. 2012; McGuire et al. 2014), few have addressed the erosion of spatter-rich vent-proximal edifices, or the effects of spatter on the erosion of vent-proximal edifices. During eruptive activity, spatter cones may partially collapse, rafting cone material away from the vent within clastogenic flows (Holm 1987; Sumner 1998), or

they may erode after the cessation of the eruption (Swanson et al. 1975). Alternatively, welded spatter interbedded with scoria can form erosion-resistant layers that slow the erosion rate of cinder cones (Wood 1980b; Dohrenwend et al. 1986). Steep slopes within the crater, or capping material composed mostly of welded spatter, may also collapse as rockfalls depositing talus, which is different than erosion mechanisms described in models of cinder cone degradation (Fodor and Németh 2015). It is therefore important to correlate the depositional facies of a spatter-rich vent edifice with the different modes and rates of degradation.

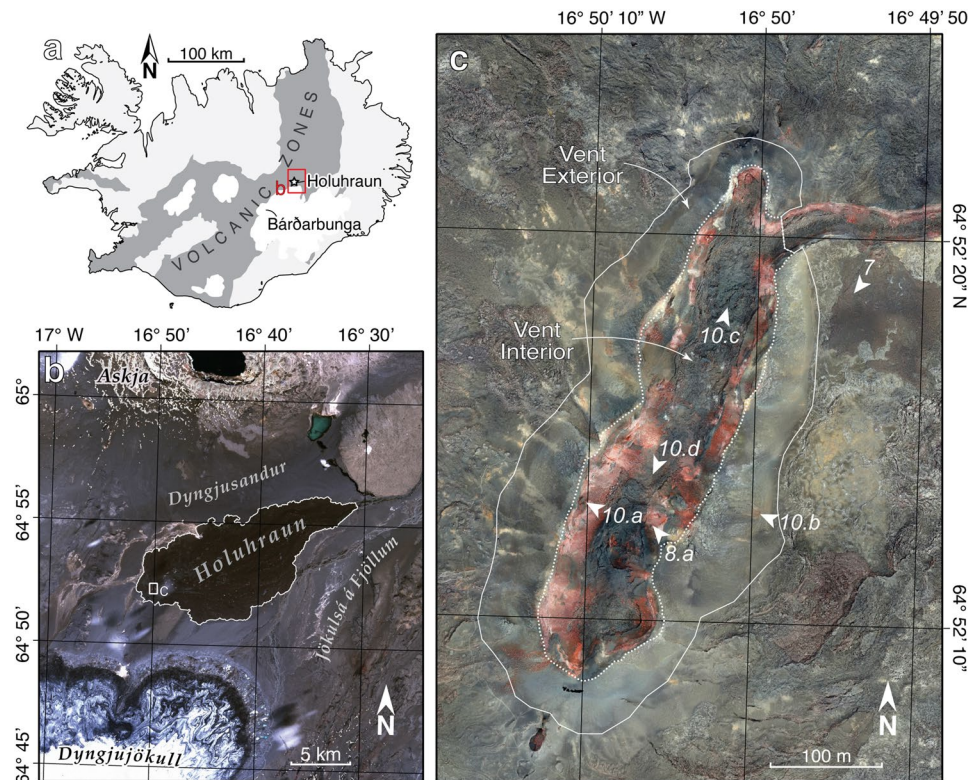
The 2014–2015 Holuhraun eruption

The Holuhraun basaltic fissure eruption occurred at the boundary of the Northern and Eastern Volcanic Zones of Iceland (Fig. 1a), and was active from August 28, 2014, to February 27, 2015 (Gudmundsson et al. 2014; Sigmundsson et al. 2015). Lava fountains erupted along a ~2-km-long fissure that formed coincident with a line of cones from a previous eruption, also called Holuhraun, that occurred during the 1860s (Hartley and Thordarson 2013; Sigmundsson et al. 2015). Within the first week of the eruption, lava fountaining focused along the fissure to form several cone structures (Witt et al. 2018). The eruption emplaced 1.44 km³ bulk volume of lava (or 1.2 km³ dense rock equivalent; Bonny et al. 2018) in a lava flow-field that extends 18 km, covering 84 km² (Fig. 1b; Hoskuldsson et al. 2016; Pedersen et al. 2017). A large spatter rampart formed along the main vent, which became the source for most of the lava emplaced during the 6-month eruption (Pedersen et al. 2017; Witt et al. 2018). The largest of the vent-proximal edifices, called Baugur, is an elongate structure that maintained a lava lake that fed the bulk of the Holuhraun lava flow field (Fig. 1c; Eibl et al. 2017; Pedersen et al. 2017; Witt et al. 2018). Baugur is made up of at least three cones that coalesced along the fissure, forming a rampart 500 m long within the first several days of the eruption, and ultimately growing to a height of ~50 m (Witt et al. 2018).

Data and methods

We conducted terrestrial laser scanning (TLS) and unoccupied aircraft system (UAS) surveys of the vent region in the first five years immediately following the cessation of the Holuhraun eruption. From these surveys, we derived a time series of high-resolution topography, enabling precise measurement of topographic changes. Rates and styles of erosion were quantified in change maps derived from topographic differencing. The processing steps described below are illustrated in Fig. S1.

Fig. 1 **a** Geologic and geographic context of Holuhraun in central Iceland, situated in the volcanic zone just north of the subglacial Bárðarbunga volcano. **B** Landsat 8 Operational Land Imager scene acquired July 4, 2020. The Holuhraun lava flow is outlined in white, with location of the Baugur vent indicated by the small rectangle marked **c**. **c** Orthophoto mosaic of Baugur derived from 20 cm unoccupied aircraft system (UAS) data (“[Aerial topographic surveys](#)”). White solid and dotted lines indicate the boundaries of the Vent Exterior and the Vent Interior, respectively. Locations of field photos in Figs. 7, 8, and 10 marked in **c** with look directions indicated by white arrows



Time series LiDAR surveys

Four TLS surveys were collected during the summers of 2015, 2016, 2018, and 2019. Each survey consisted of overlapping scans from a tripod-mounted Riegl VZ-400 laser scanner with a horizontal range of 400 m. TLS surveys were generated from individual light detection and ranging (LiDAR) scans geolocated using a Trimble R8 Global Navigation Satellite System (GNSS) base station positioned along the rim of the vent and a matching R8 rover that was mounted on top of the Riegl scanner. GNSS receivers communicated during the real-time kinematic (RTK) survey with an internal horizontal positioning accuracy of 0.06–1.40 cm (Table S1). Individual scans were collected in a 360° cylindrical grid pattern with a vertical extent of 100° (30–130° from vertical), and an angular separation of laser shots of either 0.02° or 0.04°, resulting in a ~4- or ~7-cm point spacing at 100 m range, respectively. Scan positions within the study area were spaced approximately every 50 to 70 m to acquire overlapping coverage and to minimize obscurations due to rugged topography.

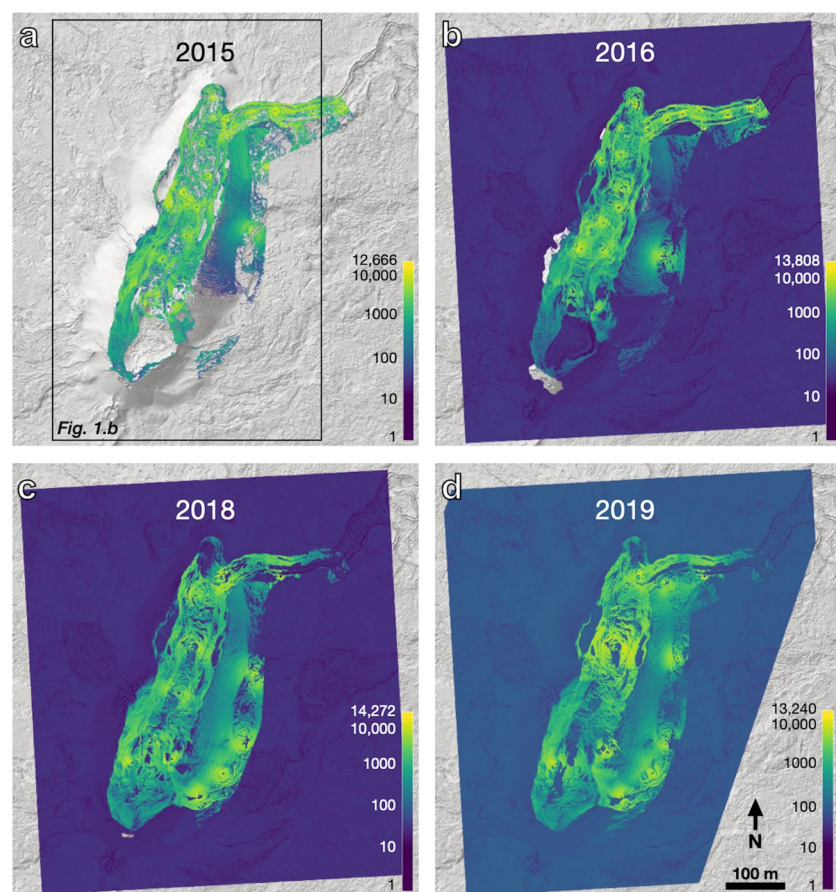
Scans of the vent interior, within the vent-proximal channel, and of the eastern exterior slope of the vent-proximal edifice comprise each year’s TLS survey (e.g. Fig. 2a). Point clouds from each scan position were registered to each other to correct for position errors using a least squares matcher on plane patches derived from the point cloud using RiScan Pro Multi-Station Adjustment (MSA; Riegl 2013). Scan

registration offsets were minimized using an iterative closest point (ICP) algorithm (Rusinkiewicz and Levoy 2001; Ullrich et al. 2003). The resulting error of these corrections is described by the standard deviation of the least squares solution for alignment of all scans for a given year, which for our scans ranged from 9 to 17 mm (Whelley et al. 2023). In addition to the statistics derived from MSA, the quality of the solution was validated by visually inspecting the overlapping portions of the scan point clouds to ensure that the adjustment computed by the software was physically meaningful and correct. Finally, the scans were combined into a single point cloud, filtered from the native point density to 2-cm spacing, exported in LAS format, and georeferenced to the UTM Zone 28N (WGS 84 datum) coordinate system using the Point Data Abstraction Library (PDAL Contributors 2018).

Aerial topographic surveys

To expand photographic and topographic coverage of Baugur, aerial surveys were collected concurrently with the LiDAR data in 2016, 2018, and 2019 using a Trimble UX5-HP fixed-wing UAS (Cosyn and Miller 2013) equipped with a Sony α7R digital single-lens reflex camera with a 15-mm lens. The UAS acquired images at 1–4 cm/pixel from 90 to 120 m above ground level. Images were precisely georeferenced using differential global positioning system (dGPS) data collected with an on-board GNSS receiver, inertial measurement unit (IMU), and a Trimble R10 base station.

Fig. 2 Merged point cloud density by year overlaid on a shaded relief map from the 2018 UAS-derived DTM (grayscale). Colors represent the number of points/m³ on a logarithmic scale. **a** 2015 coverage included TLS data only. **b** 2016 merged UAS and TLS data. UAS point data is generated from a raster at a grid spacing of ~20 cm (note two ~100 m long data gaps on the west and south flanks). **c** 2018 merged TLS–UAS point cloud (note one small data gap on the south flank). **d** 2019 merged TLS–UAS data, with the UAS point grid spacing at ~12 cm



The aerial images were bundle adjusted in the Trimble Business Center photogrammetry module to generate 20 cm/pixel or 12 cm/pixel digital elevation models (DEM) and 4 cm orthoimage mosaics covering the vent region (Table S1).

Elevation data synthesis

Topographic datasets from TLS and UAS were combined into a merged point cloud for 2016, 2018, and 2019 providing data coverage of the vent region (Fig. 2b–d; Sutton et al. 2023). Topographic dataset merging was performed in CloudCompare v2.11 (CloudCompare 2021). For each year, TLS point clouds were imported into CloudCompare, and gridded UAS DEMs were imported as point clouds, where each raster pixel defined a vertex in Cartesian space. The cloud-to-cloud (C2C) comparison tool within CloudCompare was used to perform a rigid transformation of the UAS data to align it to the TLS point cloud. An initial run of C2C provided preliminary information about areas where topographic changes had likely occurred. Subregions of areas where significant topographic changes had occurred were masked out. The unmasked regions were run through C2C again, resulting in a transformation matrix that was then applied to the entire UAS point cloud to bring it into

alignment with the TLS point cloud. The aligned UAS data were then merged with the TLS point clouds to effectively fill any gaps of 10 cm or greater in the TLS dataset, preserving all TLS vertices and extending coverage beyond the TLS surveys.

Final merged TLS–UAS point clouds underwent minor rotations (<0.5° in X and Y, and <<1° in Z) and translations (on the order of a few meters in X, Y, and Z) to co-register all point clouds. The merged TLS–UAS point cloud for 2016 was registered to the 2015 TLS point cloud by default, as the 2016 TLS point cloud was registered to the 2015 TLS point cloud. As the extent of the UAS coverage is much greater than the TLS coverage, later point clouds required minor shifts to achieve a relative adjustment for 2018 and 2019 to match the 2016 merged data.

Relative error in registering each pair of merged point clouds was determined by performing a statistical analysis of areas where changes were assumed to be minimal. The larger areas were primarily located in the terrain outside of the vent exterior, which was only covered only by UAS data. Small portions of the vent floor that showed minimal elevation differences were extracted to include areas with LiDAR-only coverage in the error analysis.

As a final processing step, to enable year-over-year volume change comparisons, points below overhangs were removed by removing points >50 cm lower than the maximum elevation point in a 20-cm planform neighborhood of each point. Although these areas constituted a very minor part of the topography, and were sparse in the point clouds, elevation difference values resulting from these points overestimated negative volume changes. These distances were determined through visual inspection of point clouds in CloudCompare to maximize the identification of underhanging surfaces while minimizing the removal of points at high-sloped but not overhanging surfaces. Overhang removal was necessary to calculate volume change, which assumed vertical elevation changes between point clouds were due to mass wasting and not complex topography.

Difference quantification

Topographic changes were identified by comparing merged point clouds from each year using the CloudCompare plugin *Multiscale Model to Model Cloud Comparison* (M3C2; Lague et al. 2013). M3C2 has been successfully used to measure topographic changes at landslides (Lague et al. 2013; James et al. 2017; Williams et al. 2019) and within volcanic vents (Hanagan et al. 2020). This method has several advantages over other point cloud differencing tools, such as C2C. For example, data gaps in either of the two point clouds being compared return no data in the M3C2 difference map, rather than producing an interpolated result. For this analysis, elevation differences between the point clouds were calculated in the vertical (+Z) direction. We used the M3C2 uncertainty value to filter points at high uncertainty/low density, which corresponded to overhangs and sub-vertical faces where poor UAS coverage provided ambiguous topography. A linear filter preserved point density with low uncertainty and filtered out points with high uncertainty.

Topographic changes were expected to be resolvable at or below the scale of the meter-sized boulders found throughout the vent interior. To ensure that measured differences were larger than the intrinsic uncertainties in the merged point clouds, differences were calculated on a subset of the point cloud (M3C2 “core points”) at an effective ground sample spacing of 10 cm. Distances between the two point clouds were measured within a diameter of 1 m centered on normal vectors computed at every core point with a maximum depth search column of 20 m. The resulting difference maps were projected onto the former and latter years’ topography to produce two difference maps for each temporal pair. For example, the M3C2 differences projected onto the 2015 topography retained the initial topography before subsequent mass wasting events, so the slopes of the “before” state could be calculated. The M3C2 differences projected

onto the latter year’s topography allowed the post-change slopes to be calculated. Changes measured in M3C2 were compared to elevation and slope. Calculation of topographic slope was performed on the point clouds within CloudCompare by calculating normal vectors using a planar fit with a 1-m diameter, oriented in the +Z direction. Slope was then assigned in degrees (0–90°) to each point as a scalar value.

After vertical changes were calculated using M3C2, the areal footprints of all points were calculated by producing Voronoi diagrams of each study year’s point cloud. Voronoi diagrams (Voronoi 1907) are used to calculate tessellated polygonal cells centered on points in 2D (or 3D in this case) space. The area of each Voronoi polygon was calculated and assigned to a central point. As virtually all points are assigned a scalar value in M3C2 describing vertical elevation change, volume change at each point was calculated through a trivial multiplication of elevation change and polygon area.

Results

We first present an overview of the elevation differences over time, spanning Baugur and the immediate vicinity, to assess the characteristics of areas where changes do and do not occur (“[Elevation change time series](#)”). We then perform a quantitative assessment of volume changes for the interior and exterior of Baugur (“[Volume change analysis](#)”). “[Exterior](#)” considers the volume changes in exterior portion of Baugur. In “[Interior](#)”, we present measurements of rockfall events on the interior walls. Finally, we correlate rockfall distributions over time with lithologic facies in “[Correlation with lithologic facies](#).”

Elevation change time series

The elevation difference map output from M3C2 shows areas where material has been removed or deposited (Fig. 3). Each difference map illustrates the patterns of mass movement, showing that discrete areas of negative and positive changes dominate the interior, while more diffuse changes of smaller magnitude occur on the exterior slopes. Negative elevation changes along the rim and exterior slopes of the rampart qualitatively appear greatest in the 2016–2018 comparison map (Fig. 3b); however, that map encompasses the cumulative differences over 2 years. The cumulative change map from 2015 to 2019 captures all changes that can be measured where only TLS coverage exists (Fig. 3d). Cumulative changes across the entire structure and surroundings are shown in the 2016–2019 map (Fig. 3e).

An overall decrease in elevation is visible on both the eastern exterior slopes (where both TLS and UAS coverage exists in 2016–2019) and on the western exterior slopes

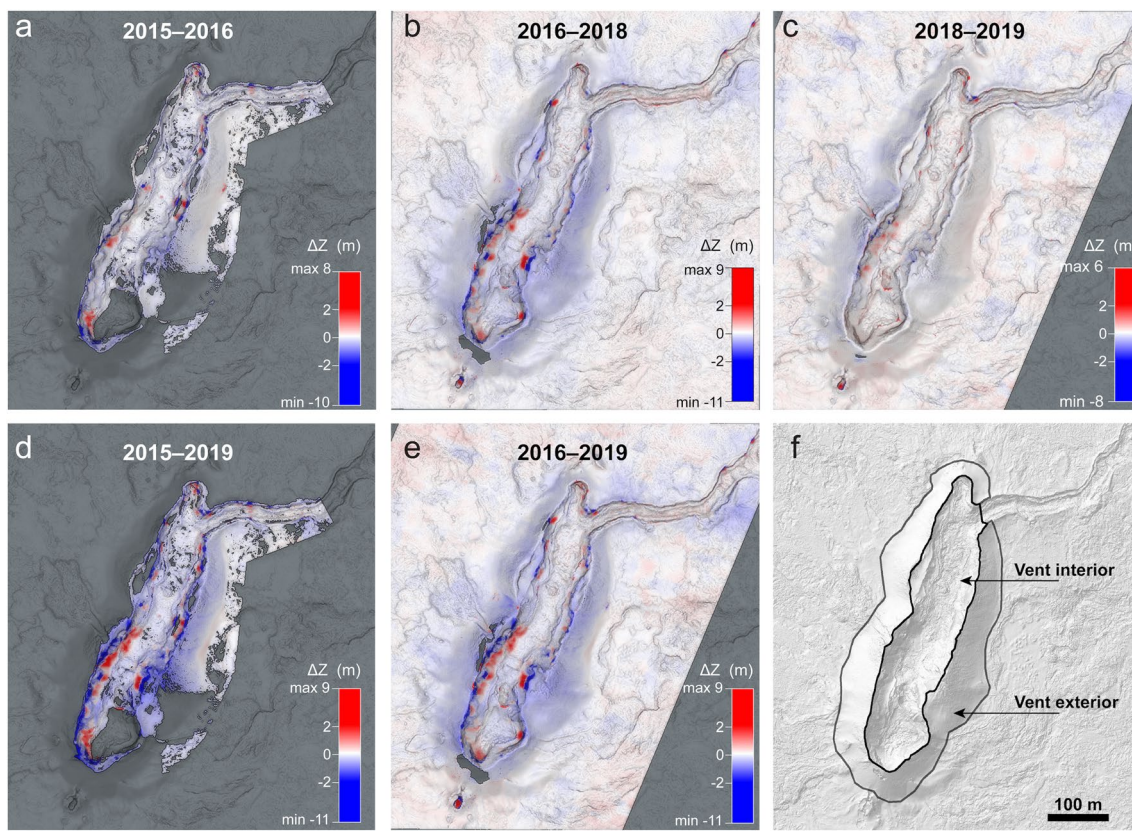


Fig. 3 Topographic changes in the Z (vertical) direction. Maps are shown stretched to the same color ramp, saturated at ± 2 m, with each map's minimum and maximum change indicated. Blue indicates negative elevation change; red indicates a positive elevation change. White indicates no change. Change maps are overlaid on merged point clouds from 2018 and 2019 (shown in dark gray) and artificially

shaded to indicate relief. **a–c** Year-to-year changes. Note that **b** spans 2 years. **d** Total cumulative change over 2015–2019, which includes TLS coverage only. **e** Cumulative change over 2016–2019, which includes merged UAS and TLS coverage. **f** Outlines of the vent exterior and interior areas drawn on the 2018 orthoimage mosaic, indicating the subset areas analyzed in Figs. 4 and 5

(which only was covered in the UAS data). Areas outside of the vent (captured in the 2016, 2018, and 2019 UAS data) show no significant change. The floor of the vent shows a cumulative (2015–2019) negative elevation change of up to -0.36 ± 0.04 m that is not apparent in the surrounding areas adjacent to the vent. The trend in negative elevation change along the vent floor is largest at the southern end and decreases towards the northern end and channel outlet. Cumulative elevation change on the exterior slopes ranges from -1.5 ± 0.04 m to 0.27 ± 0.04 m. The largest magnitude elevation changes are observed as discrete patches along the interior vent walls, likely due to rockfalls and corresponding talus deposition. The largest magnitude elevation changes from 2015 to 2019 occur within these rockfalls, and range from -10.92 m to 9.73 ± 0.04 m.

Volume change analysis

We extracted total volume changes (derived from the elevation change maps) for each time step difference map over the area encompassing Baugur. We further divided the vent edifice into two subareas: the vent interior and the vent exterior (Fig. 3f). The channel forms a break in the vent exterior unit where it exits the vent to the northeast. The vent interior boundary includes the head of the channel but does not extend into the channel. The boundary was drawn across the channel outlet to include only areas that relate to the construction of the spatter rampart. Channel wall construction was governed by different processes, such as levee formation by overbank flows (Lipman and Banks 1987), and therefore are not included in this study.

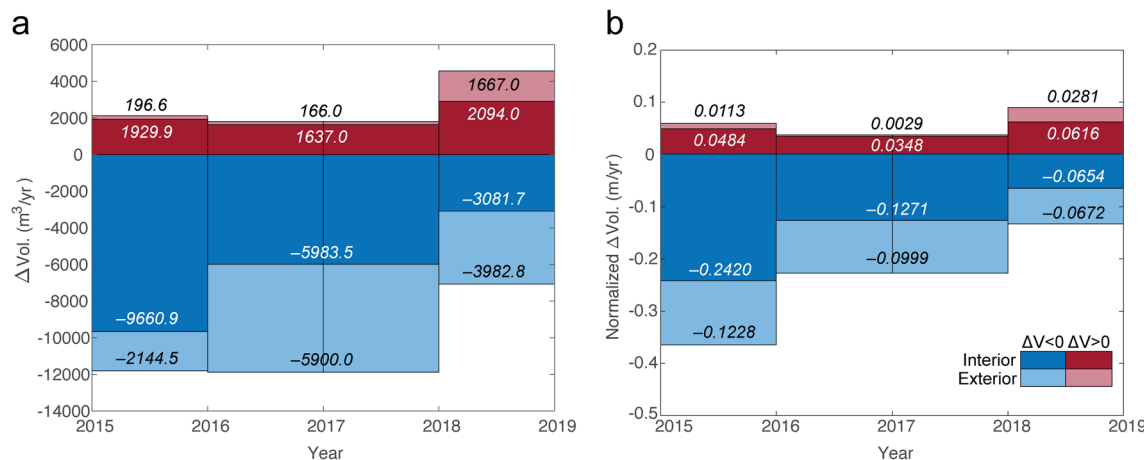


Fig. 4 Average volume change per year for the interior and exterior portions of Baugur, showing the larger magnitude of negative change compared to positive change, and the decreasing trend in negative change from year-to-year. Also note the magnitude of changes are larger on the vent interior than on the exterior. Height of stacked

bars represents the total negative or positive volume change. **a** Total change (m^3/year). **b** Volume changes normalized by the area of each sub-area (interior or exterior). The magnitude of the normalized change can be interpreted as average elevation change per year

The total sum of volume changes from the interior and exterior areas shows the magnitude of the total negative change decreasing over the 4-year time span of the study (Fig. 4a). Furthermore, the magnitude of the negative changes is greater than that of the positive changes. The magnitude of positive volume change, however, does not show a clear trend; it decreases slightly over the 2016–2018 timestep, but increases in the 2018–2019 timestep. The contribution of the interior and exterior negative volume changes is more balanced in 2018–2019 than in other years.

To account for the lower spatial coverage in the 2015–2016 change map, the sum of volume changes at each timestep was normalized by the area of the point clouds within each segment (Fig. 4b). Normalized values show similar trends—the positive changes are several times lower than the negative changes, the negative changes decrease in magnitude over time, and positive changes increase in the 2018–2019 timestep. Normalized volume changes show a greater volume loss from the exterior slopes from 2015 to 2016, decreasing to slightly less than that of the volume loss over the interior slopes during 2016–2018. Deposition on the exterior slopes is consistently lower than on interior slopes.

Volume changes derived from the elevation change maps show trends with topographic slope and elevation (Fig. 5). The exterior slopes show that most deposition occurs on slopes $<40^\circ$. The largest negative and positive volume changes on the vent exterior occur over the 20–40° slopes. This is expected since the range of slope angles on the exterior is predominantly within that range. The negative volume change is greater on the exterior slopes during 2015–2016, decreasing during the 2016–2018 period, and then maintaining

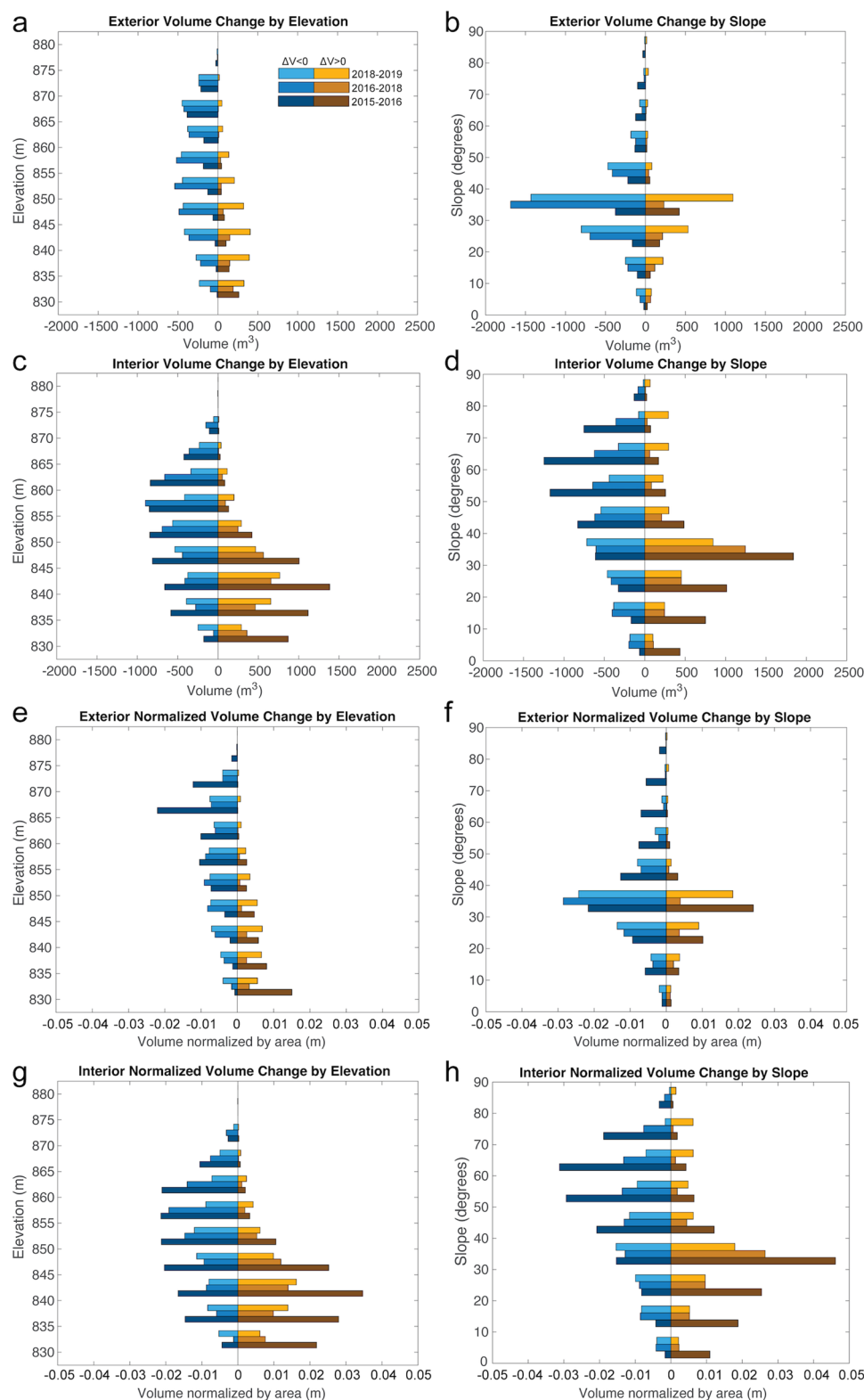
approximately the same rate of change during 2018–2019. The positive volume change on the exterior slopes is greatest in 2018–2019, particularly on slopes from 20 to 40°. The interior of the vent shows a volume change distribution that is strongly negative at higher slopes with greater positive change on lower angle slopes. The greatest positive change in the interior is in the 30–40° bin in all years.

Exterior

Over the cumulative time span of 2015–2019, the elevation along the upper exterior portion of the rampart shows a decrease of >1 m compared to the total deposition at the base of the exterior slope of <0.2 m (Fig. 6). Volume changes on the exterior slopes correlate strongly with elevation and are greatest during the first timestep (2015–2016; Fig. 5a, e). The correlation with slope (Fig. 5b, f) for the exterior is more symmetrical, with the peak negative and positive changes occurring in the 30–40° range. This correlation reflects the topography, as the mean of the exterior slopes for 2016, 2018, and 2019 is 31° with a standard deviation of 11°.

Slope measurements were derived from the merged point cloud topography. The exterior surfaces are variable in roughness, and therefore at short baselines, slope measurements show some variability. However, there are clear correlations with facies and topographic slope. The exterior portion of Baugur shows exposures of agglutinated spatter along the rim and upper ~1/3 of the rampart. Slopes along the upper exterior portion of the rampart measure ~45–55°, which is steeper than the static angle of repose for unconsolidated granular material and is at the minimum of the range for cohesive material (Beakawi Al-Hashemi and Baghabra

Fig. 5 Average volume **a–d** and elevation **e–h** change per timestep, binned by elevation (**a, c, e, g**) and slope (**b, d, f, h**). In general, volume changes decrease in magnitude from year-to-year. On the interior, more negative changes occur on higher slopes, with greater positive changes on lower slopes, indicating mass movement from the higher to lower slopes. Exterior changes correlate more strongly with elevation. Volume calculations have been shifted by the mean elevation change for each timestep. Binned volume changes for 2016–2018 represent averages per year over the 2-year timestep. Exterior (**a, b, e, f**) and Interior (**c, d, g, h**) subareas refer to the outlined areas in Fig. 3. Binned volume changes (**a–d**) were normalized by dividing by the area within each region (Interior and Exterior) (**e–h**)



Al-Amoudi 2018). These measurements are consistent with our field observations that the material composing the upper portion of the rampart is coherent. The surface of the middle section of the exterior shows interbedded spatter and scoria,

with slopes ranging from $\sim 34^\circ$ down to $\sim 31^\circ$. The base of the exterior is predominantly loose scoria, and shallows to slopes $< 31^\circ$ (Fig. 7).

Interior

We identified rockfalls in the vent interior portion of each difference map point cloud as discrete patches of negative change observed above a corresponding area of positive change. The UAS-derived orthomosaics from 2016, 2018, and 2019 were used to confirm rockfalls identified in the difference maps. Each group of points identified as a rockfall was segmented in CloudCompare by identifying the negative volume changes bounded by areas of no change. The selected 3D points were outlined with a convex hull around a best-fit plane and saved as polygons that could be projected onto a 2D map (“[Correlation with lithologic facies](#)”).

Fig. 6 Mean change in elevation versus elevation binned in 5-m increments from the 2019–2015 difference map, over the eastern exterior slopes from the rim to the base. The elevation change is negative over nearly the entire slope area, with a slight positive change near the base. The change per bin decreases with elevation, exhibiting a concave-down curve, indicating a greater loss in volume over the (vertically) highest part of the edifice. Error bars are the standard deviations (1σ) for each bin

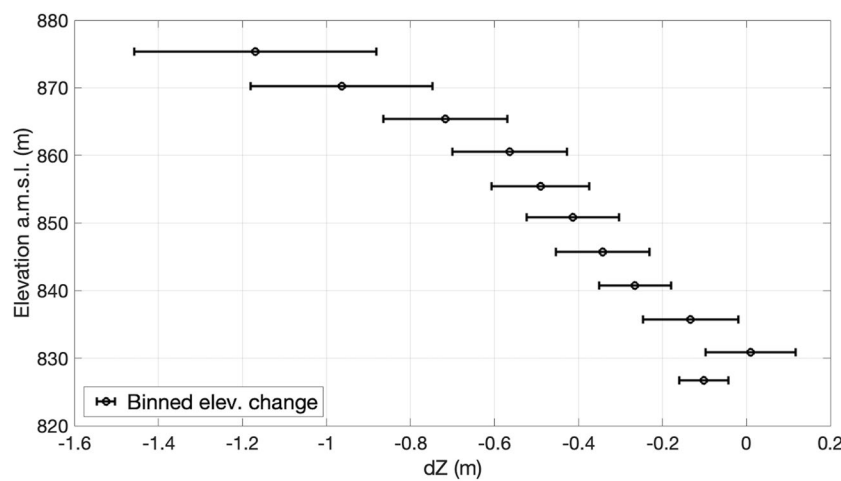


Fig. 7 The eastern exterior of Baugur, looking southwest. The upper ~1/3 and rim consists primarily of agglutinated spatter. The middle range of the rampart exterior consists of intermixed scoria and spatter, and the lower portion is primarily unconsolidated scoria. Slope degree measurements indicated were obtained from the merged TLS–UAS point cloud. Photo credit, Lis Gallant

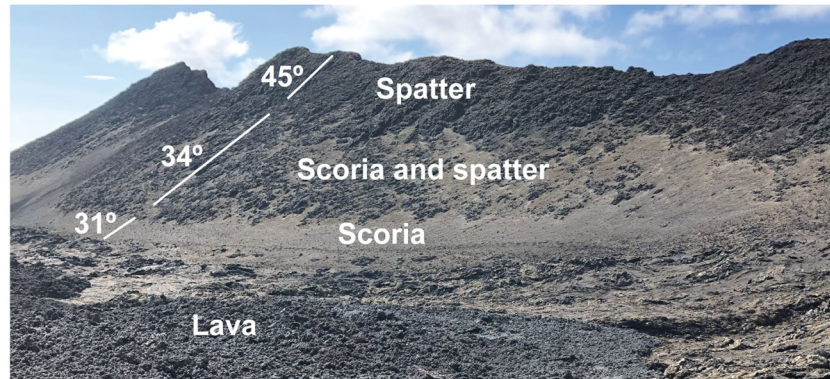


Table 1 Cumulative rockfall mapped volume statistics from each change map. Note that the number and volumes of the 2016–2018 interval spans 2 years

Timestep	N	Total Vol. (m ³)	Minimum (m ³)	Maximum (m ³)	Mean (m ³)	Std. Dev. (m ³)
2015–2016	169	7110.0	0.49	1918.9	42.1	167.6
2016–2018	174	5029.1	0.09	648.7	28.9	75.6
2018–2019	130	1246.7	0.23	112.9	9.6	18.8

Rockfalls generally initiated at higher elevations and on oversteepened slopes (Fig. 5b, d), corresponding to areas composed of welded spatter deposited during the later stages of vent construction (Witt et al. 2018). Most of the upper interior slopes have been affected by rockfalls, which are observed to reoccur at the same location from year-to-year. The volumes for all mapped rockfalls range from 0.1 to 1918.9 m³ (Table 1). The volume represented by each rockfall patch likely includes multiple events as the temporal resolution of our difference maps only allows for the recording of cumulative effects over 1- or 2-year intervals (Barlow et al. 2012).

The material released from each rockfall event was redistributed on talus slopes built up on top of the lava

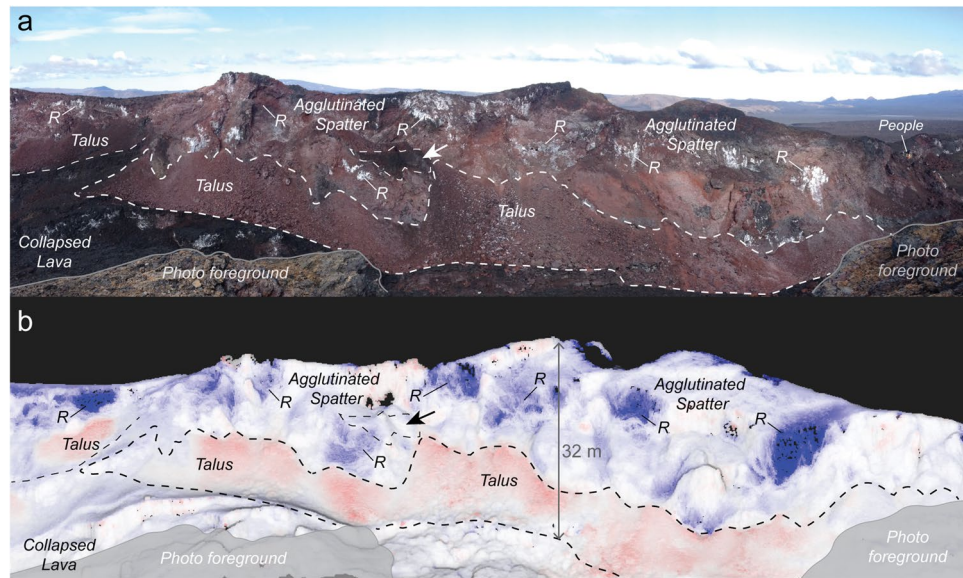


Fig. 8 **a** Field photo from 2019 looking towards the interior western wall. **b** Similar perspective view of the volume difference map between the 2019 and 2016 point clouds projected onto 2019 topography. Volume change colors are saturated at $\pm 0.1 \text{ m}^3$. Blue indicates negative change. Red indicates positive change. White indicates no change. Black indicates no data. In both **a** and **b**, example rockfall

patches are marked with the letter *R*. *Collapsed Lava*, *Agglutinated Spatter*, and *Talus* units correspond to mapped units in Fig. 9. Dashed lines show selected areas in both scenes. The white and black arrows in **a** and **b**, respectively, identify a dark patch of spatter, which is unchanged between years

ledges and ramps along the interior walls of the vent (Fig. 8). Minimal amounts of material from rockfalls have reached the vent floor. Patches of light-toned mineralization are often visible where wall material has been removed by rockfall events (Fig. 8a). Exposed wall material remains oversteepened (as of 2019), apparently leaving it prone to future failure as evidenced by the overlapping rockfalls mapped from year-to-year.

Correlation with lithologic facies

We mapped vent facies based on the 2018 UAS data produced at 0.04 m/pixel (Fig. 9b). Units were determined by delineating areas based on slope and roughness properties derived from the 2018 topographic model and confirmed by interpreting the 2018 orthomosaic. Unit descriptions were also informed by our field observations (Fig. 10). *Agglutinated Spatter* corresponds to areas of higher roughness and steeper slopes ($\sim 36^\circ$ – 50°). *Agglutinated Spatter* occurs along the rim and upper slopes of the vent. *Transitional Spatter* is interbedded scoria and spatter and makes up most of the middle section of the outer slopes. The slopes of the *Transitional Spatter* unit range from ~ 30 to 36° . The base of the exterior is mapped as *Scoria*; the slope angles in the scoria unit are at or near the angle of repose for unconsolidated granular material

(~ 25 – 30° ; Beakawi Al-Hashimi et al. 2018). The *Talus* unit represents rubbly piles of reddish unconsolidated material and primarily occurs along the inner walls of Baugur below the *Agglutinated Spatter* unit. The *Talus* unit does not extend to the floor of the vent. Talus piles and rockfalls are a unit that has formed since the end of eruptive activity and are a product of vent degradation. The *Collapsed Lava* unit is composed of dark gray slabs of the lava crust that remained after the lava drained via the northern channel. Flat-lying units adjacent to the base of the vent are mapped as *Scoria Mantle*. Remnant channels are mapped as *Rubbly Pahoehoe* (Keszthelyi et al. 2004; Voigt et al. 2021).

Rockfalls correlate strongly with the *Agglutinated Spatter* unit (Fig. 9b). Outlines of the mapped rockfall areas are projected onto the 2D facies map as polygons (Fig. 9a, b). The apparent overlap of polygons from the same year is an artifact of the convex hull fit to the 3D points identified for each rockfall. The polygons from different years do overlap, showing that rockfalls can reoccur in the same location. The facies mapping and rockfall mapping were conducted independently, lending support to the correspondence of rockfalls to the *Agglutinated Spatter* unit. The majority of talus from the rockfalls has accumulated on the ledges along the interior walls, that thus far has prevented burial and infilling of the vent floor.

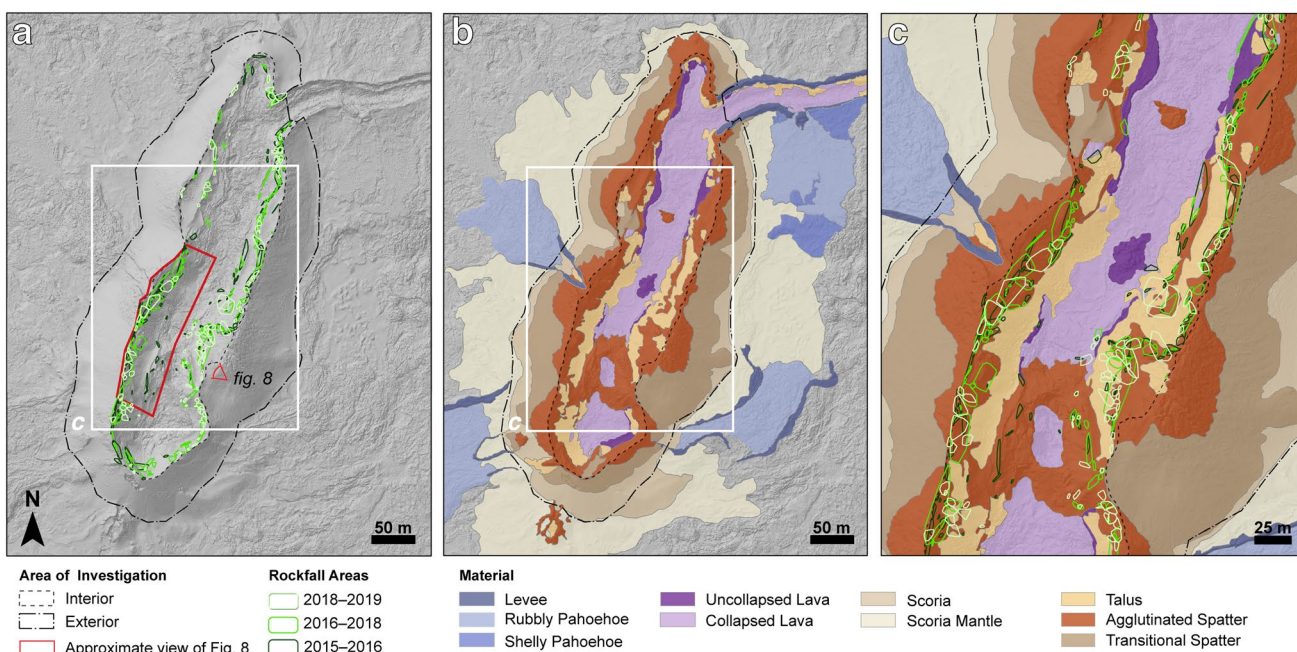


Fig. 9 **a** Rockfall outlines mapped by timestep. **b** Facies map of Baugur and immediate vicinity highlighting spatter, *Scoria*, *Collapsed Lava* (interior) and *Uncollapsed Lava* (exterior) units. **c** Inset detail of rockfall outlines overlaid on the facies map. Mapped rockfalls show a clear correlation between year-to-year rockfalls and the *Agglutinated*

Spatter unit. Black dotted and dot-dashed outlines indicate the vent interior and exterior analysis areas. The basemap in all panels is the shaded relief derived from the 2018 UAS topography. The red outline in **a** indicates the approximate area shown in the perspective view in Fig. 8 as viewed from the location of the eye symbol

Discussion

Observations of topographic changes at Baugur over 5 years reveal that exterior slopes and interior walls degrade by different processes. One of the most notable results of the difference maps is that volume is not conserved (i.e. the negative topographic changes are greater than the positive topographic changes). This is an unexpected result, because material removed by erosion (e.g. via rockfalls or gravitational sliding) should be balanced by a corresponding positive volume change (deposition). This implies that processes other than the downslope movement of material may be contributing to the observed negative elevation change. To separate the part of the signal due to mass wasting from other potential causes of negative elevation change, we first balanced the positive and negative total changes by assuming equal mass balance. Ostensibly, the remainder would represent negative elevation changes due to non-mass wasting processes.

Negative elevation changes that are not compensated by equivalent positive elevation changes could be due to physical processes such as graben subsidence, cooling contraction, sedimentary compaction, and/or aeolian deflation. We have adjusted for uncertainty within our topographic data to a minimum level by only measuring changes larger than the estimated errors. The resulting percentage of the

negative changes not balanced by positive volume change is 82.7% for 2015–2016, 85.1% for 2016–2018, and 38.3% for 2018–2019 (Table 2).

It is not possible to measure or model every factor that could contribute to the observed excess negative topographic change, but we do consider data processing artifacts (“[Data uncertainties](#)”), graben subsidence (“[Graben subsidence](#)”), and thermal contraction (“[Thermal contraction](#)”). In “[Rockfalls](#),” we examine changes in the rates and magnitudes of rockfalls on the interior of Baugur. In “[Landform evolution synthesis](#),” we discuss how observed erosion processes could be incorporated into landform evolution models for volcanic vent edifices.

Data uncertainties

Errors in the merging and relative registration of the year-to-year point clouds could contribute to the apparent mass imbalance. However, if the larger negative elevation change was solely due to the merging of the LiDAR and UAS data sets, it would be unlikely to appear in the western slopes of the exterior, which were not sampled in the LiDAR surveys. The negative elevation change signal does, in fact, appear on both the east and west-facing slopes. The flat-lying terrain surrounding the vent, which was mostly covered only by the UAS data, does not display a strong negative signal;

Fig. 10 Field photos (taken from locations indicated in Fig. 1c) illustrating some of the units described in the facies map (Fig. 9b). **a** Agglutinated Spatter forming the upper rim interior wall with a Talus deposit on the interior western wall. Clasts in the foreground are ~30–40 cm. **b** Exterior eastern surface with the Agglutinated Spatter unit above the Scoria deposit. Clasts in the foreground are up to 4 cm. **c** View from the interior floor facing north showing Collapsed Lava, Uncollapsed Lava, and Talus units. Overhangs are visible in the northern interior of the vent. **d** View from the interior floor facing towards the southern end of the vent. J.A. Richardson for scale (1.8 m). Collapsed Lava slabs cover the floor of the vent, with the interior cone composed of Agglutinated Spatter noted. The view in panel **a** is indicated from the Talus unit looking up towards the rim



Table 2 Estimated negative topographic change (volume and percentage of negative change) for each timestep, above uncertainty levels. Year-to-year registration uncertainty of merged TLS and UAS point clouds is reported as the standard deviation of dZ values in non-changing areas

Timestep	Estimated uncertainty (m)	Total negative volume change (m^3/year)	Total positive volume change (m^3/year)	Excess negative volume change (m^3/year)	Excess negative volume change (%)
2015–2016	0.07	−11,328	1962	−9366	83
2016–2018	0.06	−11,694	1743	−9951	85
2018–2019	0.09	−5580	3445	−2135	38

those areas tend to have a mean difference in the M3C2 difference maps that is slightly positive (~0.01 m). Minor photogrammetric artifacts appear in the surrounding terrain, but their contribution is accounted for in the error level measured for each difference map (Table 2). Other artifacts result from the difference quantification, which overcounts positive value volume changes, particularly at oversteepened slopes of overhangs where the M3C2 search depth parameter unavoidably overshoots the intended reference surface. The choice of the M3C2 parameters, particularly the depth search parameter, was a tradeoff between being able to accurately capture the largest negative changes on steep slopes and inadvertently counting complex surfaces as positive

changes (“Difference quantification”). Thus, data uncertainties cannot account for the observed excessive negative volume change.

Graben subsidence

Baugur is situated along the western fault boundary of a graben (Hjartardóttir et al. 2015; Kolzenburg et al. 2021). Subsidence due to drainback of magma along the dike may seem like a candidate factor in the overall lowering of Baugur after the end of the eruption. Graben formation above the dike that sourced the Holuhraun flow was marked by an elevation drop of ~3–4 m between parallel fault lines.

This drop occurred during the initial stages of the eruption, and thereafter did not exhibit a significant lowering in repeat surveys up to the summer of 2019 (Kolzenburg et al. 2021). Ongoing graben subsidence therefore seems unlikely to be a major contributing factor to the negative elevation change observed. However, apparent subsidence of the edifice could be due to other causes, such as compaction due to thermal contraction and/or settling.

Thermal contraction

The signal of negative change is confined to the vent edifice, implying a shallow mechanism, such as thermal contraction. In studies of the cooling contraction of lava flows (Wittman et al. 2017) and pyroclastic deposits (Whelley et al. 2012), thermal contraction was modeled to derive rates of subsidence. To investigate the potential magnitude of volume loss at Baugur, we estimate volumetric change due to cooling, and compare the estimates to the difference measurements.

The change in volume for an unconstrained material can be estimated to first order simply by multiplying the initial volume, V , by a factor describing the material's response to thermal changes, α , and the change in temperature, dT (Turcotte and Schubert 2014; p. 204),

$$dV = V \times \alpha \times dT. \quad (1)$$

Similarly, when considering just the change in height (dZ), the formula can be written as

$$dZ = Z \times \gamma \alpha \times dT, \quad (2)$$

where the scaling coefficient, γ , would be 1 for the 1D linear function (as in Eq. 1), and 3 for the case where the only volumetric contraction is in the height direction (Wittman et al. 2017). However, as the vent edifice is not a slab of constant thickness, and the actual change is likely in three dimensions, we use an intermediate value for $\gamma = 1.7$, based on Chaussard (2016), where $\gamma = (1 + \nu)/(1 - \nu)$, and ν is Poisson's ratio of 0.25. Our results from the topographic differencing measured elevation changes (dZ), from which we calculated volume changes (dV). For the purposes of comparing the potential contribution of thermal contraction to the overall elevation changes (Fig. 6), we can estimate to an order of magnitude what the potential contribution of cooling might be to elevation (height, Z) changes, using Eq. (2), with $\gamma = 1.7$, to obtain a factor that describes a percentage change. The magnitude of the thermal response of basalt can vary depending on density, vesicularity, temperature, and composition (Richter and Simmons 1974). For the coefficient of thermal expansion of basalt, α , we use $8.30 \times 10^{-6} \text{ K}^{-1}$, derived from laboratory measurements of Icelandic basalts from the Hekla volcano, which included samples of various porosity over a range of temperatures comparable to

the situation at Baugur (Wittman et al. 2017). The choice for dT relies on assumptions based on observations of the initial and final temperatures of the edifice spanning the time of our observations. We observed completely welded deposits lower in the vent and agglutinated spatter along the upper portion and rim, implying that deposition temperatures were hot enough for clasts to be deformable and sticky, but were lower than the eruption temperature. The deposition temperature can be estimated to be near the glass transition temperature of 725 °C (Ryan and Sammis 1981). When completely cooled, the solidified lava would be at the ambient air temperature. Although the surface was cool enough to walk on at least as early as six months after the end of the eruption (i.e. at the time of our initial survey), fumarolic activity was observed during each year of our surveys, implying that subsurface temperatures in at least some portions of Baugur were at least 100 °C as late as 2019. Although temperatures of up to 1195 °C were measured during the 2014–2015 eruption (Kolzenburg et al. 2017), we conservatively bracket the range of dT for the welded clasts with a maximum of 725 °C – 0 °C = 725 °C, to a minimum of 725 °C – 100 °C = 625 °C. We find that the maximum estimated elevation change due to cooling contraction is –0.07 m if the material cooled completely to ambient temperature. The more realistic value for dT , 625 °C, yields a maximum elevation change of –0.06 m. These estimates compare reasonably well to the observed average decrease in elevation of a few tens of centimeters over the ~50 m height of the rampart, demonstrating that thermal contraction is likely to be responsible for roughly 50% of the observed negative elevation changes (Fig. 11).

Compaction may also contribute to observed volume changes due to settling of unconsolidated tephra or by degassing of residual clastogenic melt within the edifice (Whelley et al. 2012; Chaussard 2016). Nonetheless, the role of thermal contraction is expected to play an important role in observed volume changes and may serve as a catalyst for mass wasting as cooling causes the development of fine-scale contraction joints that weaken steep welded spatter, thereby enhancing gravitational instability and increasing the likelihood of rockfalls. As new surfaces are exposed by rockfalls, it is also possible that the cooling processes that form cracks may be migrating deeper into the edifice, propagating instabilities into the edifice.

Rockfalls

The number of cataloged rockfall events decreases only slightly from year-to-year, while the total volume and maximum size rockfall both decrease more dramatically. Rockfall total volumes decrease from 7110 m³ in 2015–2016 to 5028 m³ over 2016–2018 (2 years) to 1247 m³ in 2018–2019 (Table 1). It is probable that each mapped rockfall event

Fig. 11 Binned elevation change from 2015 to 2019 over the eastern exterior slope (Fig. 6) compared to the estimated contribution of negative elevation change due to thermal contraction. The red lines are the result of Eq. 2 calculated with $\gamma = 1.7$, $\alpha = 8.30 \times 10^{-6}$ K^{-1} , and $dT = 625^\circ$ (solid line) and 725° (dashed line)

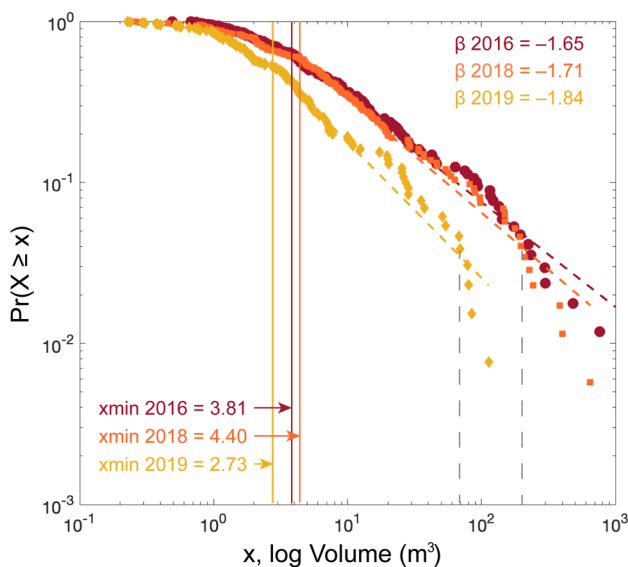
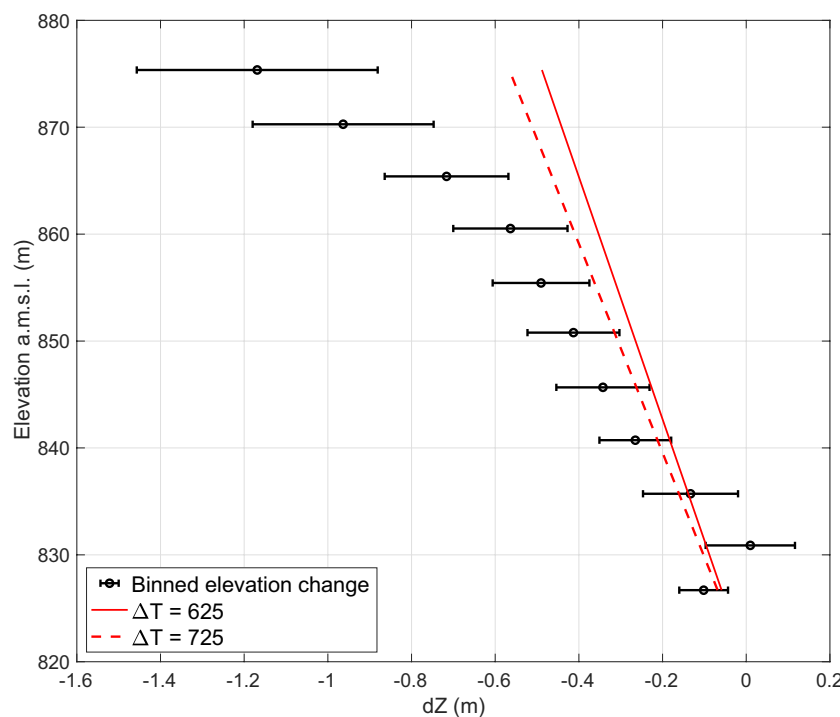


Fig. 12 Complementary cumulative distribution function of rockfalls normalized by time interval (2015–2016, maroon circles; 2016–2018, orange squares; 2018–2019, yellow diamonds). The beta (β) value is the slope of the power law fitted to each time step (dashed lines) for rockfall volumes greater than the cutoff size, x_{min} (m^3), indicated by the solid vertical lines. The minimum cutoff and β values were calculated using code from Clauset et al. (2009). Gray dashed vertical lines indicate approximate locations where the data deviate from the fitted function at the larger end of the distribution for 2019 ($\sim 70 m^3$) and 2016–2018 ($\sim 200 m^3$)

represents the cumulative effect of multiple smaller events, as they were not observed in real time (Hovius et al. 1997; Barlow et al. 2012). Even so, the overall trend of decreasing rockfall volume implies that the relative contribution of smaller events is increasing in time. This implication is borne out in the complementary cumulative distribution function (CCDF) of rockfall data for each timestep (Fig. 12) that shows the scaling value (β) of the power law fit is >1 in absolute magnitude (Barlow et al. 2012). The power law fit is only applied to volumes greater than a calculated cut-off value using the method of Clauset et al. (2009). Visual inspection of the CCDF shows that using the power law fit to extrapolate to larger volumes could overestimate the likelihood of larger magnitude events occurring in the future as the fit to the distribution is not well correlated at the larger end of the data set. The apparent threshold for what would be considered a good fit at the larger end of the distribution is $\sim 200 m^3$ within the first three years, and $\sim 70 m^3$ in the fourth year. The similarity of the plots for the first two time steps (2015–2016 and 2016–2018, spanning the first three years), and the marked difference thereafter indicates some physical process changed resulting in a decrease of the largest rockfall volumes. The reduction in rockfall magnitude may be an effect of diminishing supply of available material at exposed over-steepened surfaces (i.e. the largest volumes collapsed within the first 3 years, reducing the available amount of gravitationally unstable material), or talus is gradually burying the exposed wall faces, which naturally buttresses the exposed, if still oversteepened walls, or it may be a combination of both factors.

We observe that rockfalls scars remain over-steepened and that rockfalls can reoccur at the same locations (Fig. 9). In many cases, rockfall scars appear to expose bright mineral deposits left by fumarolic activity (Fig. 8a; Achilles et al. 2019). This apparent correlation may be explained by fumarolic activity degrading the rock strength by hydrothermal alteration (Darmawan et al. 2022). Weakly agglutinated spatter contacts in the material deposited in the upper portion of the vent edifice may also be prone to degradation due to fumarolic activity, promoting collapse where there is already instability due to over-steepened slopes (cf. Hanagan et al. 2020). It is likely that rockfalls will continue as long as there are gravitationally unstable surfaces available, suggesting the value of continued monitoring to identify ongoing hazards.

Landform evolution synthesis

Our observations of Baugur indicate that spatter-rich edifices degrade by different modes than are described by the landform evolution models for cinder cones, which assume that diffusion is the dominant degradation process (Wood 1980b; Pelletier and Cline 2007). Ideal diffusive processes would be expected to show a signature of balanced positive change (deposition) as non-cohesive material moves from higher to lower elevations, resulting in the gradual shallowing of slopes (Pelletier and Cline 2007). In reality, volume may not be conserved locally. For example, some loss of volume may be expected due to aeolian removal. Fornaciai et al. (2010) noted a deficit in the volume of deposited material of up to 75% of the volume eroded from the upper exterior slopes of Etnean cinder cones, which they attributed to wide dispersal by wind, with lack of agglutination noted as a contributing factor. We observed that downslope movement of unconsolidated material on the edifice exterior was hindered by the presence of spatter along the upper portion of the edifice. However, slight deposition was observed at the exterior base, due to the downslope movement of scoria from the middle and lower slopes (Fig. 7).

The more striking divergence from the diffusive degradation model occurs on the interior of the vent edifice. Over time, rockfalls along the vent interior walls convert coherent pyroclastic deposits (agglutinated spatter) into unconsolidated material. Yet this material forms relatively large (tens of centimeter to ~1 m), highly angular clasts that form stable talus deposits (Fig. 10a) which were not prone to further downslope movement during the first 5 years. Downslope movement of talus in the vent interior may progress in a two-stage process such that initial deposition occurs onto the ledges by talus until it reaches the angle of repose, at which point material can advance further downslope and begin infilling the crater floor. It may be that once the accommodation space on the ledges is filled, talus will be deposited on

the vent floor. However, we did not observe any significant accumulation of material on the floor of the vent during the five years after the eruption ceased. Additional topographic surveys, potentially spaced at intervals of ~5 years, would be necessary to confirm this prediction.

The magnitude of elevation change at rockfall locations was on the order of a few meters, with cumulative change from 2015 to 2019 up to 11 m in some areas. As the wall material was removed, the rim retreated horizontally and vertically by up to ~3 m in places (Fig. 13a). The upper interior walls maintained oversteepened slopes, rather than developing into gradually shallower slopes. Over a longer time span, the cumulative effects of episodic interior rockfalls may resemble a more diffusive process (Fig. 13b), but on short timescales (<5 years), they may primarily represent the products of discrete events that have not reached statistical equilibrium. Our observations suggest that a hybrid model would better describe the modes of degradation that occur during the earliest stages of evolution of spatter ramparts.

Conclusions

We documented the initial stages of degradation of the primary vent (Baugur) of the 2014–2015 Holuhraun eruption in northern Iceland, finding that up to 24,710 m³ of material was eroded from the interior walls and 17,927 m³ was removed from the exterior slopes, for a total volume loss of 42,637 m³ over the period from 2015 to 2019. Positive volume change (deposition) in the vent interior was 8108 m³, and on the exterior 2196 m³ was deposited for a total of 10,304 m³. Volume changes are a result of two distinct styles of erosion. Material in the interior of the vent is removed from oversteepened slopes by discrete rockfalls, burying the ledges below in talus. Minimal material had accumulated on the floor of the vent 5 years after the cessation of the eruption (Figs. 10c,d and 13b). Diffusive processes are qualitatively evident on the edifice exterior in the topographic change maps, but measurements are below the estimated level of uncertainty. Material is hindered from eroding from the rim and upper portions of the exterior slopes by a capping rim of cohesive spatter deposits and interbedded spatter and cinders. We estimate that bulk contraction due to cooling could contribute to a maximum of a few tens of centimeters decrease in elevation. However, cooling contraction alone cannot fully explain the observed imbalance in the negative volume changes. Other mechanisms such as compaction-induced settling of the edifice and/or aeolian transport and deflation are required to explain the mass balance change over the edifice.

We propose a conceptual landform evolution model that combines stochastic rockfall processes on the interior walls,

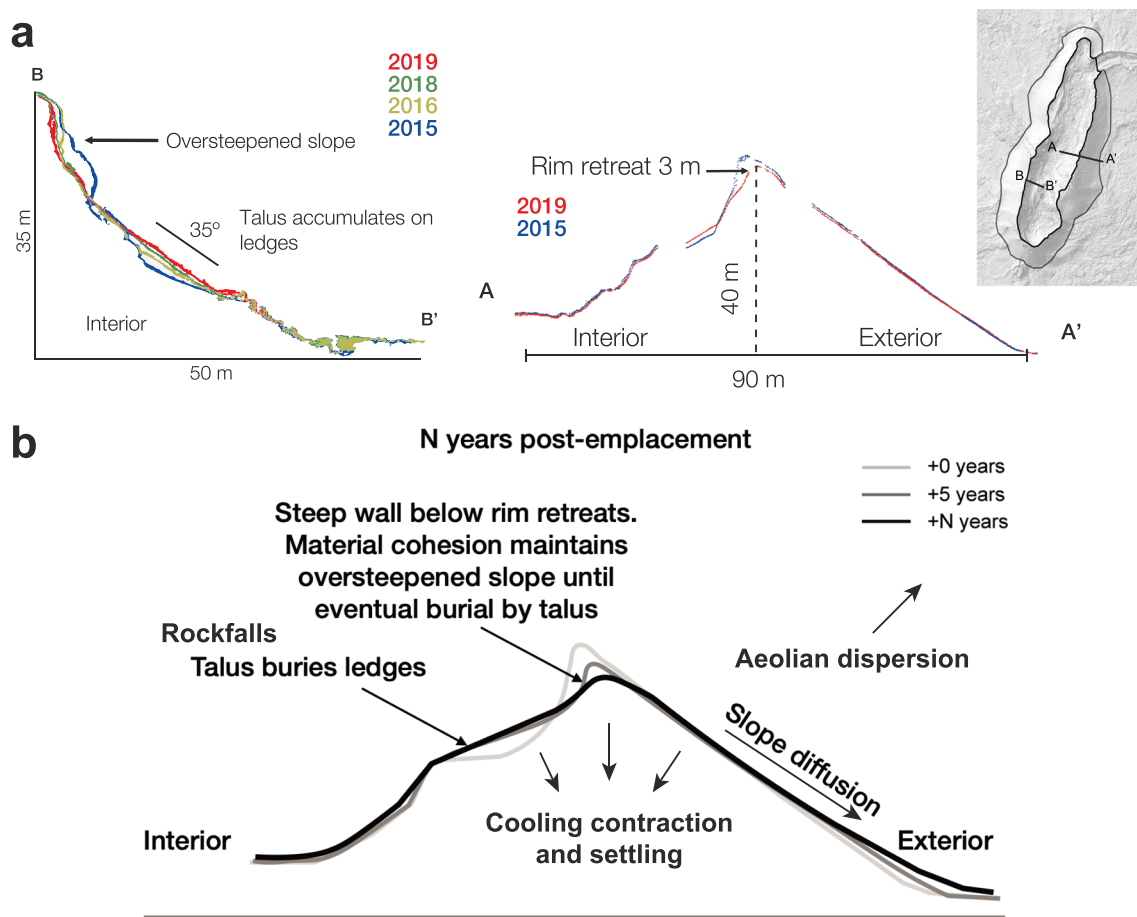


Fig. 13 **a** Topographic profiles from A–A' and B–B' indicated on inset overview of change map from 2015 to 2019. The progression of slope changes shows where large rockfalls occurred between 2015 and 2016, with smaller rockfalls occurring in subsequent years. **b**

Hypothetical morphological evolution of the spatter rampart over N years based on the observed changes on the interior and exterior slopes within the first five years after the eruption ended

diffusive gravitational sliding on the portions of exterior slopes where unconsolidated scoria exists, and that also incorporates cooling contraction and compaction over the entire edifice to better describe the observed modes of degradation the earliest stages of evolution of spatter ramparts, or spatter-rich scoria cones. The occurrence of discrete mass wasting events trends towards smaller magnitude events, possibly evolving to more diffusive processes. Our observations support a model where the vent diameter widens relatively quickly after the eruption ceases, inviting comparison to models of impact craters and other steeply sloped, gravitationally unstable landforms in the Solar System (Fassett and Thomson 2014; Fassett et al. 2017). Our conceptual model fills a gap in landform evolution models for volcanic vents both in terms of the composition (spatter-rich) and in the description of processes occurring during the very earliest stages of degradation.

Potential hazards at Baugur and similar fresh volcanic vents primarily impact visitors (e.g. tourists, researchers,

and park staff) hiking in and around the vent area. Collapses along the crater rim and rockfalls inside the vent are the greatest hazards that we identified in the data presented here. The difference maps show clearly that rockfall events occurred each year and can reoccur at previous rockfall locations. Areas of steep slopes are prone to gravitational instability, particularly as the contacts between welded spatter clasts degrade due to a combination of factors including thermal contraction, weathering, fumarolic activity, and settling. The areas with the highest erosion rates correlated to the highest elevations (i.e. along the rim). Talus deposits appear to be stable and less prone to further mass wasting. The temporal span of this study is not sufficient to make reliable predictions about the ongoing hazard potential. However, the data can be used to inform the cadence of repeat surveys that would be sufficient to adequately monitor the evolution of spatter ramparts or similar vent edifices, such as annual surveys conducted for the first few years, followed by repeat surveys at longer intervals thereafter.

Supplementary Information The online version contains supplementary material available at <https://doi.org/10.1007/s00445-024-01709-9>.

Acknowledgements Many thanks to those who assisted with LiDAR data collection in the field, including Shane Byrne, Andrew de Wet, Debra Needham, Lis Gallant, Alexandra Huff, Joana Voigt, and the students in the Keck Research Experiences for Undergraduates (REU) program who participated in 2016. Many thanks to Ármann Höskuldsdóttir, Thorvaldur Thórðarson, and Ingibjörg Jónsdóttir, of the University of Iceland, for facilitating field work at Holuhraun and Baugur. All field work within the Vatnajökull National Park (Vatnajökulsþjóðgarður) was conducted under valid scientific research permits. We express our gratitude to the rangers at the Vatnajökull National Park Service for sharing their expertise, and to the camp wardens at Dreki. This work also benefited from valuable discussions with the Goddard Volcano Writing Group and Jeffrey Andrews-Hanna. We thank Alison Graettinger and one anonymous reviewer for their constructive and helpful comments that greatly improved this manuscript.

Funding Partial support for field work and data analysis was provided by the Goddard Instrument Field Team (GIFT) Internal Scientist Funding Model. SSS was partially supported by the National Science Foundation Graduate Research Fellowship Program (Grant #DGE-1746060). PLW and SPS were supported in part by NASA award #80GSFC21M0002, administered by the Center for Research and Exploration in Space Science and Technology, NASA/GSFC, Greenbelt, MD. PLW was also supported in part by the NASA Postdoctoral Program. CWH was partially supported by the NASA Planetary Science and Technology through Analog Research program (Grant #80NSSC21K0011) and by the NASA Planetary Geology and Geophysics program (Grant #NNX14AL54G).

Open Access This article is licensed under a Creative Commons Attribution 4.0 International License, which permits use, sharing, adaptation, distribution and reproduction in any medium or format, as long as you give appropriate credit to the original author(s) and the source, provide a link to the Creative Commons licence, and indicate if changes were made. The images or other third party material in this article are included in the article's Creative Commons licence, unless indicated otherwise in a credit line to the material. If material is not included in the article's Creative Commons licence and your intended use is not permitted by statutory regulation or exceeds the permitted use, you will need to obtain permission directly from the copyright holder. To view a copy of this licence, visit <http://creativecommons.org/licenses/by/4.0/>.

References

- Achilles CN, McAdam AC, Knudson CA, Young KE, Bleacher J, Bower D, Eigenbrode J, Hamilton C, Hewagama T, Nixon C, Richardson J, Scheidl S, Sutton S, Voigt J, Wasser M, Whelley N, Whelley P (2019) Acidic alteration in a young basaltic lava field: sulfur-bearing products and implications for Mars. In: 50th Lunar and Planetary Science Conference, Abstract #3043. LPI Contribution
- Barlow J, Lim M, Rosser N et al (2012) Modeling cliff erosion using negative power law scaling of rockfalls. *Geomorphology* 139–140:416–424. <https://doi.org/10.1016/j.geomorph.2011.11.006>
- Beakawi Al-Hashemi HM, Baghabra Al-Amoudi OS (2018) A review on the angle of repose of granular materials. *Powder Technol* 330:397–417. <https://doi.org/10.1016/j.powtec.2018.02.003>
- Bemis KG, Ferencz M (2017) Morphometric analysis of scoria cones: the potential for inferring process from shape. In: Németh K, Carrasco-Núñez G, Aranda-Gómez JJ, Smith IEM (eds) Monogenetic Volcanism. The Geological Society of London, London, pp 61–100
- Bemis K, Walker J, Borgia A et al (2011) The growth and erosion of cinder cones in Guatemala and El Salvador: models and statistics. *J Volcanol Geotherm Res* 201:39–52. <https://doi.org/10.1016/j.jvolgeores.2010.11.007>
- Bonny E, Thordarson T, Wright R, Höskuldsson A, Jónsdóttir I (2018) The volume of lava erupted during the 2014 to 2015 eruption at Holuhraun, Iceland: a comparison between satellite- and ground-based measurements. *J Geophys Res Solid Earth* 123:5412–5426. <https://doi.org/10.1029/2017JB015008>
- Cas R, Wright J (2012) Volcanic successions modern and ancient: a geological approach to processes, products and successions. Springer Science & Business Media
- Chaussard E (2016) Subsidence in the Parícutin lava field: causes and implications for interpretation of deformation fields at volcanoes. *J Volcanol Geotherm Res* 320:1–11. <https://doi.org/10.1016/j.jvolgeores.2016.04.009>
- Clauset A, Shalizi CR, Newman MEJ (2009) Power-law distributions in empirical data. *SIAM Rev* 51:661–703. <https://doi.org/10.1137/070710111>
- CloudCompare version 2.11.3 (2021) GPL software. Retrieved from <http://www.cloudcompare.org/>. Accessed 3 September 2023
- Cosyn P, Miller R (2013) Trimble UX5 aerial imaging solution—a new standard in accuracy, robustness and performance for photogrammetric aerial mapping. White Paper. Available online at <https://www.semanticscholar.org/paper/Trimble-UX5-Aerial-Imaging-Solution-Cosyn-Miller/2bd7fad8fb7107eb4e0192d0c95726ad3b639ac5>. Accessed 3 September 2023
- Darmawan H, Troll VR, Walter TR et al (2022) Hidden mechanical weaknesses within lava domes provided by buried high-porosity hydrothermal alteration zones. *Sci Rep* 12:3202. <https://doi.org/10.1038/s41598-022-06765-9>
- Dohrenwend JC, Wells SG, Turpin BD (1986) Degradation of Quaternary cinder cones in the Cima volcanic field, Mojave Desert, California. *GSA Bull* 97:421–427
- Eibl EPS, Bean CJ, Jónsdóttir I et al (2017) Multiple coincident eruptive seismic tremor sources during the 2014–2015 eruption at Holuhraun, Iceland. *J Geophys Res Solid Earth* 122:2972–2987. <https://doi.org/10.1002/2016JB013892>
- Fodor E, Németh K (2015) Spatter cone. *Encycl. Planet. Landforms* 2028–2034
- Fassett CI, Thomson BJ (2014) Crater degradation on the lunar maria: topographic diffusion and the rate of erosion on the Moon. *J Geophys Res Planets* 119:2255–2271. <https://doi.org/10.1002/2014JE004698>
- Fassett CI, Crowley MC, Leight C et al (2017) Evidence for rapid topographic evolution and crater degradation on Mercury from simple crater morphometry. *Geophys Res Lett* 44:5326–5335. <https://doi.org/10.1002/2017GL073769>
- Fornaciai A, Behncke B, Favalli M et al (2010) Detecting short-term evolution of Etnean scoria cones: a LiDAR-based approach. *Bull Volcanol* 72:1209–1222. <https://doi.org/10.1007/s00445-010-0394-3>
- González de Vallejo LI, Hernández-Gutiérrez LE, Miranda A, Ferrer M (2020) Rockfall hazard assessment in volcanic regions based on ISVS and IRVS. *Geomechanical Indices. Geosciences* 10:220. <https://doi.org/10.3390/geosciences10060220>
- Gudmundsson A, Lecoer N, Mohajeri N (2014) Dike emplacement at Bardarbunga, Iceland, induces unusual stress changes, caldera deformation, and earthquakes. *Bull Volcanol* 76:1–7. <https://doi.org/10.1007/s00445-014-0869-8>
- Hanagan C, La Femina PC, Rodgers M (2020) Changes in crater morphology associated with volcanic activity at Telica Volcano, Nicaragua. *Geochemistry, Geophysics, Geosystems* 21:1–15. <https://doi.org/10.1029/2019GC008889>

- Hartley ME, Thordarson T (2013) The 1874–1876 volcano-tectonic episode at Askja, North Iceland: lateral flow revisited. *Geochemistry, Geophys Geosystems* 14:2286–2309. <https://doi.org/10.1002/ggge.20151>
- Hauber E, Bleacher J, Gwinner K et al (2009) The topography and morphology of low shields and associated landforms of plains volcanism in the Tharsis region of Mars. *J Volcanol Geotherm Res* 185:69–95. <https://doi.org/10.1016/j.jvolgeores.2009.04.015>
- Head JW, Wilson L (1989) Basaltic pyroclastic eruptions: influence of gas-release patterns and volume fluxes on fountain structure, and the formation of cinder cones, spatter cones, rootless flows, lava ponds and lava flows. *J Volcanol Geotherm Res* 37:261–271. [https://doi.org/10.1016/0377-0273\(89\)90083-8](https://doi.org/10.1016/0377-0273(89)90083-8)
- Hjartardóttir ÁR, Einarsson P, Gudmundsson MT, Högnadóttir T (2015) Fracture movements and graben subsidence during the 2014 Bárðarbunga dike intrusion in Iceland. *J Volcanol Geotherm Res* 310:242–252. <https://doi.org/10.1016/j.jvolgeores.2015.12.002>
- Holm RF (1987) Significance of agglutinate mounds on lava flows associated with monogenetic cones: an example at Sunset Crater, northern Arizona. *Bull Geol Soc Am* 99:319–324. [https://doi.org/10.1130/0016-7606\(1987\)99<319:SOAMOL>2.0.CO;2](https://doi.org/10.1130/0016-7606(1987)99<319:SOAMOL>2.0.CO;2)
- Hooper DM, Sheridan MF (1998) Computer-simulation models of scoria cone degradation. *J Volcanol Geotherm Res* 83:241–267. [https://doi.org/10.1016/S0377-0273\(98\)00031-6](https://doi.org/10.1016/S0377-0273(98)00031-6)
- Hoskuldsson A, Jonsdottir I, Thordarson T (2016) Futurvold and the Bardarbunga eruption 2014–15 Iceland, success in the field and laboratory. In: EGU General Assembly, Geophysical Research Abstracts, p 13687
- Hovius N, Stark CP, Allen PA (1997) Sediment flux from a mountain belt derived by landslide mapping. *Geology* 25:231–234. [https://doi.org/10.1130/0091-7613\(1997\)025<0231:SFFAMB>2.3.CO;2](https://doi.org/10.1130/0091-7613(1997)025<0231:SFFAMB>2.3.CO;2)
- James MR, Robson S, Smith MW (2017) 3-D uncertainty-based topographic change detection with structure-from-motion photogrammetry: precision maps for ground control and directly georeferenced surveys. *Earth Surf Process Landforms* 42:1769–1788. <https://doi.org/10.1002/esp.4125>
- Kereszturi G, Jordan G, Németh K, Dóniz-Páez JF (2012) Syn-eruptive morphometric variability of monogenetic scoria cones. *Bull Volcanol* 74:2171–2185. <https://doi.org/10.1007/s00445-012-0658-1>
- Keszthelyi L, Thordarson T, McEwen A et al (2004) Icelandic analogs to Martian flood lavas. *Geochemistry, Geophys Geosystems* 5:Q11014. <https://doi.org/10.1029/2004GC000758>
- Kolzenburg S, Giordano D, Thordarson T et al (2017) The rheological evolution of the 2014/2015 eruption at Holuhraun, central Iceland. *Bull Volcanol* 79. <https://doi.org/10.1007/s00445-017-1128-6>
- Kolzenburg S, Kubanek J, Dirscherl M et al (2021) Solid as a rock: tectonic control of graben extension and dike propagation. *Geology*. <https://doi.org/10.1130/G49406.1>
- Lague D, Brodus N, Leroux J (2013) Accurate 3D comparison of complex topography with terrestrial laser scanner: application to the Rangitikei canyon (N-Z). *ISPRS J Photogramm Remote Sens* 82:10–26. <https://doi.org/10.1016/j.isprsjprs.2013.04.009>
- Lipman PW, Banks NG (1987) AA flow dynamics, Mauna Loa 1984. *Volcanism in Hawaii, USGS Professional Paper*, p 1350
- McGuire LA, Pelletier JD, Roering JJ (2014) Development of topographic asymmetry: insights from dated cinder cones in the western United States. *J Geophys Res Earth Surf* 119:1725–1750. <https://doi.org/10.1002/2014JF003081>
- Moore RB, Helz RT, Dzurisin D et al (1980) The 1977 eruption of Kilauea volcano, Hawaii. *J Volcanol Geotherm Res* 7:189–210. [https://doi.org/10.1016/0377-0273\(80\)90029-3](https://doi.org/10.1016/0377-0273(80)90029-3)
- Parcheta CE, Houghton BF, Swanson DA (2012) Hawaiian fissure fountains 1: decoding deposits—episode 1 of the 1969–1974 Mauna Ulu eruption. *Bull Volcanol* 74:1729–1743. <https://doi.org/10.1007/s00445-012-0621-1>
- Parfitt L, Wilson L (2009) Fundamentals of physical volcanology. John Wiley & Sons
- PDAL Contributors (2018) PDAL Point Data Abstraction Library. <https://doi.org/10.5281/zenodo.2556738>
- Pedersen GBM, Höskuldsson A, Dürig T et al (2017) Lava field evolution and emplacement dynamics of the 2014–2015 basaltic fissure eruption at Holuhraun, Iceland. *J Volcanol Geotherm Res* 340:155–169. <https://doi.org/10.1016/j.jvolgeores.2017.02.027>
- Pelletier JD, Cline ML (2007) Nonlinear slope-dependent sediment transport in cinder cone evolution. *Geology* 35:1067–1070. <https://doi.org/10.1130/G23992A.1>
- Porter SC (1972) Distribution, morphology, and size frequency of cinder cones on Mauna Kea Volcano, Hawaii. *GSA Bull* 83:3607–3612. [https://doi.org/10.1130/0016-7606\(1972\)83\[3607:DMASFO\]2.0.CO;2](https://doi.org/10.1130/0016-7606(1972)83[3607:DMASFO]2.0.CO;2)
- Richardson JA, Bleacher JE, Connor CB, Glaze LS (2021) Small volcanic vents of the Tharsis volcanic province, Mars. *J Geophys Res Planets* 126:1–23. <https://doi.org/10.1029/2020JE006620>
- Rieg LMS (2013) RiSCAN Pro Manual. Rieg: Horn
- Richter D, Simmons G (1974) Thermal expansion behavior of igneous rocks. *Int J Rock Mech Min Sci* 11:403–411. [https://doi.org/10.1016/0148-9062\(74\)91111-5](https://doi.org/10.1016/0148-9062(74)91111-5)
- Rusinkiewicz S, Levoy M (2001) Efficient variants of the ICP algorithm. In: Proceedings Third International Conference on 3-D Digital Imaging and Modeling, pp 145–152. <https://doi.org/10.1109/IM.2001.924423>
- Ryan MP, Sammis CG (1981) The glass transition in basalt. *J Geophys Res Solid Earth* 86:9519–9535. <https://doi.org/10.1029/JB086iB10p09519>
- Segerstrom K (1956) Geologic investigations in the Parícutin area, Mexico U.S. Geological Survey Bulletin, p 965
- Settle M (1979) The structure and emplacement of cinder cone fields. *Am J Sci* 279:1089–1107. <https://doi.org/10.2475/ajs.279.10.1089>
- Sigmundsson F, Hooper A, Hreinsdóttir S et al (2015) Segmented lateral dyke growth in a rifting event at Bárðarbunga volcanic system, Iceland. *Nature* 517:7533. <https://doi.org/10.1038/nature14111>
- Sumner JM (1998) Formation of clastogenic lava flows during fissure eruption and scoria cone collapse: the 1986 eruption of Izu-Oshima Volcano, eastern Japan. *Bull Volcanol* 60:195–212. <https://doi.org/10.1007/s004450050227>
- Sumner JM, Blake S, Matela RJ, Wolff JA (2005) Spatter. *J Volcanol Geotherm Res* 142:49–65. <https://doi.org/10.1016/J.JVOLGORES.2004.10.013>
- Sutton SS, Whelley PW, Richardson JA, Scheidt SP, Hamilton CW (2023) Repeat surveys of the topography of the main vent of the 2014–2015 eruption at Holuhraun, Iceland: merged LiDAR and UAS point clouds from 2015, 2016, 2018, and 2019. University of Arizona Research Data Repository. Datasets. <https://doi.org/10.25422/azu.data.19680372>
- Swanson DA, Wright TL, Helz RT (1975) Linear vent systems and estimated rates of magma production and eruption for the Yakima Basalt on the Columbia Plateau. *Am J Sci* 275:877–905. <https://doi.org/10.2475/ajs.275.8.877>
- Turcotte DL, Schubert G (2014) Geodynamics, Third. Cambridge University Press, Cambridge, UK
- Ullrich A, Schwarz R, Kager H (2003) Using hybrid multi-station adjustment for an integrated camera laser-scanner system. In: Proceedings of Optical 3D Measurement Techniques, pp 298–304
- Valentine GA, Cortés JA, Widom E et al (2017) Lunar crater volcanic field (Reveille and Pancake Ranges, Basin and Range Province, Nevada, USA). *Geosphere* 13:391–438. <https://doi.org/10.1130/GES01428.1>
- de Vitturi MM, Arrowsmith JR (2013) Two-dimensional nonlinear diffusive numerical simulation of geomorphic modifications to cinder cones. *Earth Surf Process Landforms* 38:1432–1443. <https://doi.org/10.1002/esp.3423>

- Voigt JRC, Hamilton CW, Steinbrügge G, Scheidt SP (2021) Surface roughness characterization of the 2014–2015 Holuhraun lava flow-field in Iceland: implications for facies mapping and remote sensing. *Bull Volcanol* 83:1–14. <https://doi.org/10.1007/s00445-021-01499-4>
- Voronoi G (1907) Nouvelles applications des paramètres continus à la théorie des formes quadratiques. première mémoire: Sur quelques propriétés des formes quadratiques positives parfaites. *J Reine Angew Math* 133:97–178
- Whelley PL, Jay J, Calder ES et al (2012) Post-depositional fracturing and subsidence of pumice flow deposits: Lascar Volcano, Chile. *Bull Volcanol* 74:511–531. <https://doi.org/10.1007/s00445-011-0545-1>
- Whelley PL, Sutton S, Richardson JA, Gallant L, Hamilton C, Höskuldsdóttir Á, Needham DH, Byrne S, Huff A, De Wet A (2023) NASA GIFT Iceland Highlands: 2015–2019 Baugur LiDAR. Geological Survey data release, U.S. <https://doi.org/10.5066/P9VQPE9W>
- Williams JG, Rosser NJ, Hardy RJ, Brain MJ (2019) The importance of monitoring interval for rockfall magnitude-frequency estimation. *J Geophys Res Earth Surf* 124:2841–2853. <https://doi.org/10.1029/2019JF005225>
- Wittmann W, Sigmundsson F, Dumont S, Lavallée Y (2017) Post-emplacement cooling and contraction of lava flows: InSAR observations and a thermal model for lava fields at Hekla volcano, Iceland. *J Geophys Res Solid Earth* 122:946–965. <https://doi.org/10.1002/2016JB013444>
- Witt T, Walter TR, Müller D et al (2018) The relationship between lava fountaining and vent morphology for the 2014–2015 Holuhraun eruption, Iceland, Analyzed by Video Monitoring and Topographic Mapping. *Front Earth Sci* 6. <https://doi.org/10.3389/feart.2018.00235>
- Wood CA (1980a) Morphometric evolution of cinder cones. *J Volcanol Geotherm Res* 7:387–413. [https://doi.org/10.1016/0377-0273\(80\)90040-2](https://doi.org/10.1016/0377-0273(80)90040-2)
- Wood CA (1980b) Morphometric analysis of cinder cone degradation. *J Volcanol Geotherm Res* 8:137–160. [https://doi.org/10.1016/0377-0273\(80\)90101-8](https://doi.org/10.1016/0377-0273(80)90101-8)